Correlating STED and synchrotron XRF nano-imaging unveils the co-segregation of metals and cytoskeleton proteins in dendrites

Florelle Domart[1,2,3,4], Peter Cloetens[5], Stéphane Roudeau[1,2], Asuncion Carmona[1,2], Emeline Verdier[3,4], Daniel Choquet[3,4,6*] and Richard Ortega[1,2*#]

[1]Chemical Imaging and Speciation, CENBG, University of Bordeaux, UMR 5797, 33175 Gradignan, France;

[2]CNRS, IN2P3, CENBG, UMR 5797, 33175 Gradignan, France;

[3]Interdisciplinary Institute for Neuroscience, University of Bordeaux, 33076 Bordeaux, France;

[4]Interdisciplinary Institute for Neuroscience, Centre National de la Recherche Scientifique (CNRS) UMR 5297, 33076 Bordeaux, France;

[5]ESRF, the European Synchrotron, 38043 Grenoble, France;

[6]Bordeaux Imaging Center, CNRS UMS 3420, University of Bordeaux, INSERM US04, 33076 Bordeaux, France;

[*]D.C. and R.O. share seniority

[#]Corresponding author: ortega@cenbg.in2p3.fr

Keywords: STED, synchrotron XRF, zinc, copper, dendritic spine, tubulin, actin, hippocampal neuron

Abstract

Zinc and copper are involved in neuronal differentiation and synaptic plasticity but the molecular mechanisms behind these processes are still elusive due in part to the difficulty of imaging trace metals at the synapse level. We correlate stimulated emission depletion (STED) microscopy of proteins and synchrotron X-ray fluorescence (SXRF) imaging of trace metals, both performed with 40 nm spatial resolution, on primary rat hippocampal neurons. We achieve a detection limit for trace metals in the zeptogram level per pixel. We reveal the co-localization at the nanoscale of zinc and tubulin in dendrites with a molecular ratio of about one zinc atom per tubulin-αβ dimer. We observe the co-segregation of copper and F-actin within the nano-architecture of dendritic spines. Overall, the combination of STED super-resolution microscopy and SXRF nano-imaging indicates new functions for zinc and copper in the regulation of the synaptic cytoskeleton associated to memory formation.

INTRODUCTION

The neurobiology of trace metals such as copper and zinc is a matter of intense investigation since they are involved in neuronal differentiation and signaling processes (1-4). One fundamental question is the localization of these metals in synaptic compartments of neuronal cells. Understanding the functions of these elements requires however to correlate their localization with respect to relevant proteins in neurons. Synchrotron X-Ray Fluorescence (SXRF) imaging using hard X-ray beams, typically above 10 keV energy, is a powerful technique to investigate the cellular localization of metals since it allows the mapping of element distributions in single cells with high analytical sensitivity (5). Using Kirkpatrick–Baez (KB) focusing mirrors, SXRF has reached a record spatial resolution of 13 nm on ID16A beamline at the European Synchrotron Radiation Facility (ESRF), while maintaining a high photon flux as required for detecting trace elements (6). We have previously reported a correlative microscopy approach consisting in labeling organelles or proteins with specific fluorophores for live-cell imaging prior to SXRF imaging (7, 8). This correlative approach is limited by the spatial resolution of optical fluorescence microscopy, above 200 nm, which is larger than the spatial resolution achieved today with nano-SXRF and insufficient to resolve synaptic sub-structures. To overcome this limitation we present a method to correlate nano-SXRF with STED (STimulated Emission Depletion microscopy) performed both at 40 nm resolution.

STED microscopy has already been successfully combined to transmission electron microscopy to correlate protein localization with cell ultrastructure (9), or to atomic force microscopy to investigate protein aggregation at high spatial resolution (10). Recently, STED has been performed together with synchrotron scanning diffraction microscopy to inform about diffraction patterns in cells (11). These correlative approaches however cannot be transposed to the imaging of metals in cells since they require steps of chemical fixation known to disrupt the metal-binding equilibrium in cells (7, 12). Moreover, glass coverslips used for STED microscopy usually contain significant amounts of zinc and of some other trace metals. SXRF and STED correlative microscopy have therefore to fulfil specific requirements in terms of substrate for cell culture, and protocols for sample preparation, to avoid element contamination, loss or redistribution. With the combination of these two high resolution

imaging techniques we observe trace metals co-localization with cytoskeleton proteins at the synaptic level in rat hippocampal neurons.

RESULTS and DISCUSSION

We designed a specific protocol consisting in live-cell STED microscopy on silicon nitride (SN) substrates followed by cryogenic processing of the cells before nano-SXRF imaging as described in (fig. 1). Primary rat hippocampal neurons were cultured *in vitro* during 15 days (DIV15) on sterile SN membranes placed above an astrocyte feeder layer as adapted from Kaech & Banker (14, 15). SN membranes were designed with an orientation frame to facilitate the reproducible positioning of the samples during the correlative imaging procedure (fig. 1A). SN membranes are biocompatible, trace metal free, 500 nm thin, transparent, flat and rigid supports developed for X-ray microscopy (12, 14). To confirm that SN membranes were also adapted to STED microscopy we compared STED imaging of SiR-tubulin of hippocampal neurons grown on glass coverslips or on SN membranes, showing no difference between the two of them (fig. S1). To perform STED microscopy we stained the DIV15 primary rat hippocampal neurons with either SiR-actin, SiR-tubulin, or with SiR-tubulin and SiR700-actin together. These two far-red SiR-based fluorophores have been developed for live-cell super resolution microscopy and are based respectively on the actin ligand jasplakinolide and the tubulin ligand docetaxel (15). Confocal and STED live-cell images were obtained using a commercial Leica DMI6000 TCS SP8 X with a 93x objective at immersion in glycerol and numerical aperture of 1.3 (fig. 1B). STED images were recorded at 40 nm spatial resolution. For each region of interest (roi) the (x,y) coordinates were registered in the confocal/STED microscope setup. Then the SN membranes were plunge-frozen at -165°C and freeze-dried at -90°C under secondary vacuum before analysis on ID16A beamline at ESRF (fig. 1B). Using the coordinates of 3 reference points on the SN membrane (3 corners of the membrane relatively to the orientation frame), the new coordinates (x',y') of the roi selected during STED microscopy were calculated for the ID16A microscope setup (fig. 1A). Nano-SXRF and synchrotron X-ray phase contrast imaging (PCI) were performed with an X-ray beam size of 40 nm at 17 KeV energy (fig. 1B). Nano-SXRF, PCI, and STED microscopy images can be merged to perform multimodal correlative microscopy (fig. 1C) of chemical elements, electron density, and fluorescently labeled proteins all obtained at similar spatial resolution (<40 nm). The

alignment of the multimodal images is accurate despite the freeze drying process that can marginally alter the cell structure (fig. 1C). The limit of detection (LOD) of nano-SXRF analysis was calculated for the detected elements according to IUPAC (International Union of Pure and Applied Chemistry) guideline resulting for zinc in in a 0.007 ng.mm^{-2} LOD, corresponding to 14 zeptogram of zinc (about 130 atoms) per pixel of 40 nm x 40 nm size (Table 1).

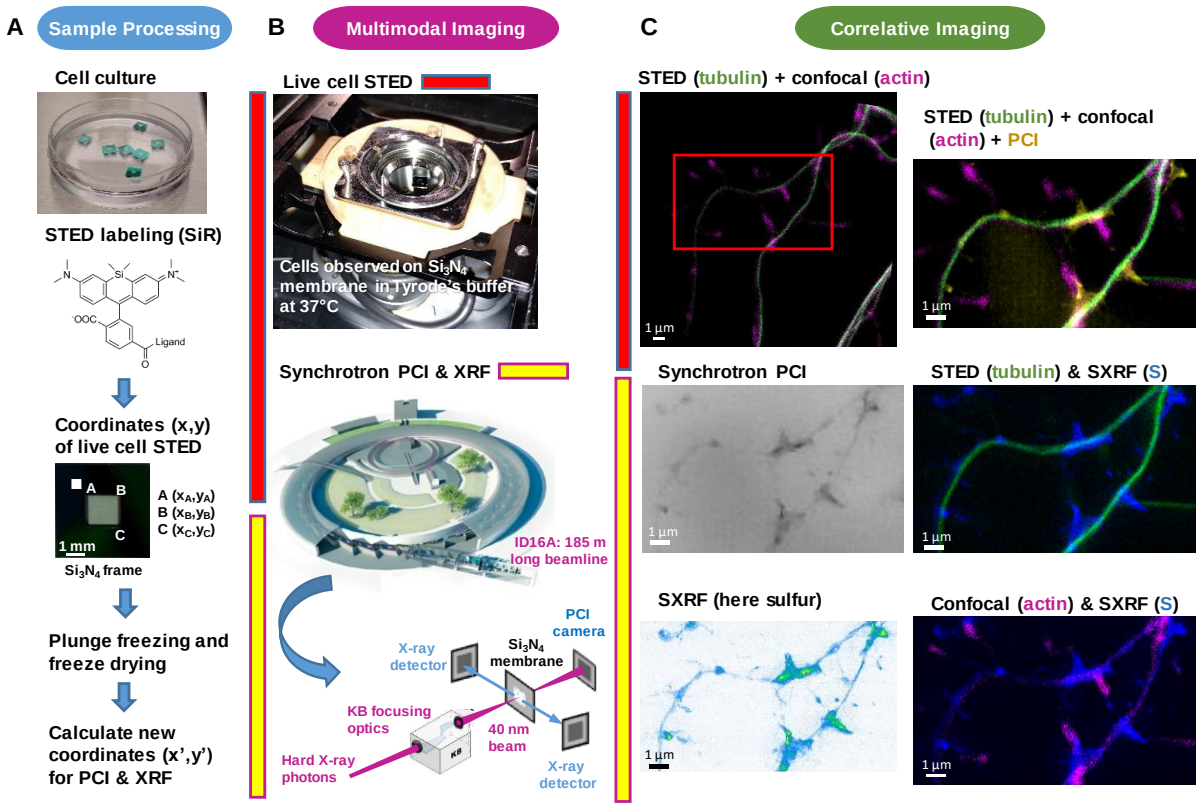

Fig. 1. Workflow for correlative STED and synchrotron multimodal nano-imaging. (A) Sample processing. Primary neurons are cultured on silicon nitride membranes and labelled with fluorescent probes designed for STED microscopy such as SiR-tubulin or SiR700-actin. STED microscopy is performed on living cells and orthonormal coordinates (x,y) of regions of interest are recorded relatively to the position of three membrane corners A, B, C identified thanks to an orientation frame. Immediately after STED microscopy cells are plunge-frozen and freeze-dried. New coordinates (x',y') of the regions of interest are calculated to perform XRF and PCI imaging on the synchrotron microscope. (B) Multi-modal imaging. Live-cell STED and confocal microscopy are performed with a Leica DMI6000 TCS SP8 X microscope equipped with a thermalized chamber. Synchrotron XRF and PCI are carried out on freeze-dried samples at ESRF on beamline ID16A. The KB optics are 185 m away from the X-ray source enabling to focus hard X-rays at 40 nm beam size. (C) Correlative imaging. Overlay images of STED, confocal, synchrotron PCI and XRF are produced on areas of few tens of µm

large with a spatial resolution of 40 nm for STED, 30 nm for PCI and 40 nm for SXRF. Several elemental maps (here sulfur) can be super-imposed with protein distributions (i.e. actin or tubulin) in dendrites and spines at 40 nm spatial resolution.

Table 1. Nano-SXRF limit of detection (LOD). LOD calculated according to IUPAC (International Union of Pure and Applied Chemistry) guideline as derived from 12 blank measurements for phosphorus, sulfur, potassium and zinc, expressed in $ng.mm^{-2}$, and expressed in g (and number of atoms) within pixels of 40 nm x 40 nm size.

	Phosphorus	**Sulfur**	**Potassium**	**Zinc**
LOD	0.331 $ng.mm^{2}$	0.095 $ng.mm^{2}$	0.080 $ng.mm^{2}$	0.007 $ng.mm^{2}$
LOD in 40 nm x 40 nm pixel	$8.2\ 10^{-19}$ g (16,000 atoms)	$2.2\ 10^{-19}$ g (4,200 atoms)	$2.4\ 10^{-19}$ g (3,800 atoms)	$1.4\ 10^{-20}$ g (130 atoms)

The highest zinc content is found in F-actin-rich dendritic spines where zinc is highly correlated with sulfur (Person's correlation coefficient > 0.6) (fig. 2-5 and S2-S4). Zinc distribution however is not fully superimposed with F-actin localization suggesting that both entities are not directly in interaction in dendritic protrusions. Zinc and sulfur hot spots are found within narrow regions in the dendritic spines characterized by the highest electron densities as shown by synchrotron PCI maps (fig. 5 and S4). This result is in agreement with the expected location of zinc in the postsynaptic density (PSD) of hippocampal synapses where zinc plays a structural function in stabilizing proteins associated to the PSD (16). Although in lower concentration than zinc, copper was also detected in F-actin rich dendritic spines showing a distinct distribution pattern than for Zn (fig. 5 and S3). In rare cases iron was also detected, as 200 nm x 100 nm structures of locally dense iron spots, in the dendrite, contiguous to the dendritic spines (fig. S4K).

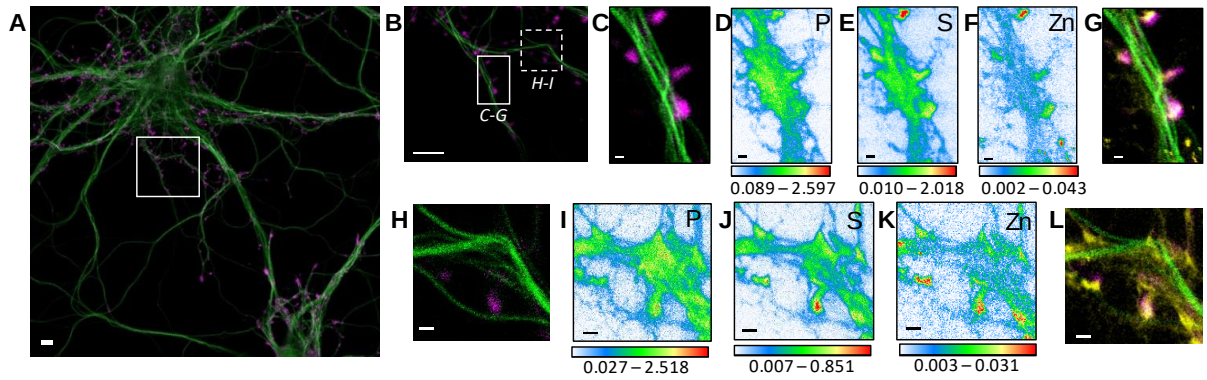

Fig. 2. Correlative STED nano-SXRF element imaging in dendritic spines. (A) Confocal image from a DIV15 primary rat hippocampal neuron stained with SiR-tubulin (green) and SiR700-actin (magenta). (B) STED image of SiR-tubulin (green) and confocal SiR700-actin (magenta) from the framed region shown in (A). (C) STED image of SiR-tubulin (green) and confocal SiR700-actin (magenta) for the region mapped by SXRF shown in (B) in plain line. (D) Phosphorus SXRF map. (E) Sulfur SXRF map. (F) Zinc SXRF map. (G) Merged images of zinc SXRF map (yellow), STED SiR-tubulin (green) and confocal SiR700-actin (magenta). (H) STED image of SiR-tubulin (green) and confocal SiR-actin (magenta) image from the framed region shown in (B) in dotted line. (I) Phosphorous SXRF map. (J) Sulfur SXRF map. (K) Zinc SXRF map. (L) Merged images of zinc SXRF map (yellow), STED SiR-tubulin (green), and confocal SiR700-actin (magenta). Scale bars: 500 nm, except (A) and (B) 5 µm. Color scale bars: min-max values in ng.mm^{-2}.

The most striking result of this correlative microscopy approach is the observation of zinc and tubulin co-localization in thin dendritic processes as illustrated in fig. 3, 4 and S3-S4. In fig. 4, a roi showing parallel microtubule filaments observed by STED microscopy was selected (fig. 4A). These parallel tubulin filaments could not be resolved by confocal microscopy (fig. 4B), but only by STED microscopy (fig. 4C). Similarly to STED microscopy, nano-SXRF performed on the same roi was able to separate the element distributions of the two thin dendritic processes (fig. 4D-E). Plot profiles of zinc and tubulin relative signal intensities across the two tubulin filaments shows the co-localization of their distributions (fig. 4F). The very good superimposition of S and Zn distributions along tubulin imaged by STED is systematically observed (fig. 3, 4K and Fig. S3-S4). The quantitative analysis of nano-SXRF data for 21 regions showing Zn and tubulin co-localization indicates that the ratio S/Zn is of 44 ± 11 (fig. 4L and Table S1). Considering that the amino acid sequence of the rat tubulin-α/β dimer contains 49 sulfur atoms per dimer, from methionine and cysteine residues, the S/Zn ratio in microtubules

corresponds to a theoretical tubulin-α/β dimer over Zn ratio of 0.9 ± 0.2 (fig. 4L). This result is in agreement with X-ray crystallography data of the tubulin-α/β dimer predicting the presence of one putative zinc ion per dimer, located in the tubulin-α subunit of zinc-induced tubulin sheets (17). Our data provided by the correlation of STED and nano-SXRF microscopy support the structural requirement for zinc in tubulin network assembly and is observed directly on cultured neurons in physiological conditions, without zinc addition. This structural role for zinc could explain why zinc is required in neuronal differentiation and facilitates tubulin polymerization (14, 18). Molecular modeling studies have also proposed such structural role for zinc in tubulin polymerization further hypothesizing that zinc dyshomeostasis, due to interactions with amyloid-beta proteins, could alter tubulin dynamics in Alzheimer's disease (19).

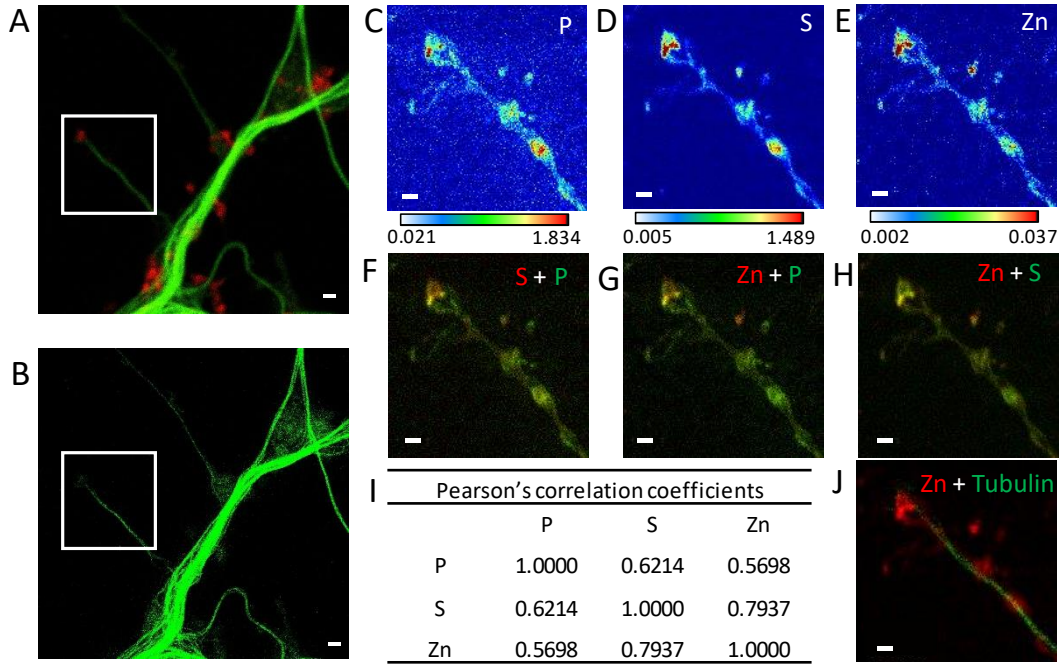

Fig. 3. Correlative imaging in dendrites and spines. (A) Confocal image of SiR-tubulin (green) and SiR700-actin (red). (B) STED image of SiR-tubulin (green) for the same zone as in (A). (C-E) SXRF element maps (P, S, Zn) from the region of interest framed in (A) and (B). (F) Overlay image of phosphorus (green) and sufur (red). (G) Overlay image of phosphorus (green) and zinc (red). (H) Overlay image of sulfur (green) and zinc (red). (I) Pearson's correlation coefficients for the elements (P, S, Zn) in the roi. (J) Overlay image of STED SiR-tubulin (green) and zinc (red). Scale bars: 500 nm, except for (A) and (B) 1 µm. Color scales min-max values in ng.mm^{-2}.

The combination of super resolution STED microscopy and nano-SXRF both performed with 40 nm resolution opens numerous perspectives of application to investigate the cell biology of metals. This correlative imaging will contribute to fill the gap between the study of protein-metal interactions in purified systems and their direct observation in cells that was limited to the sub-micrometric level up to now.

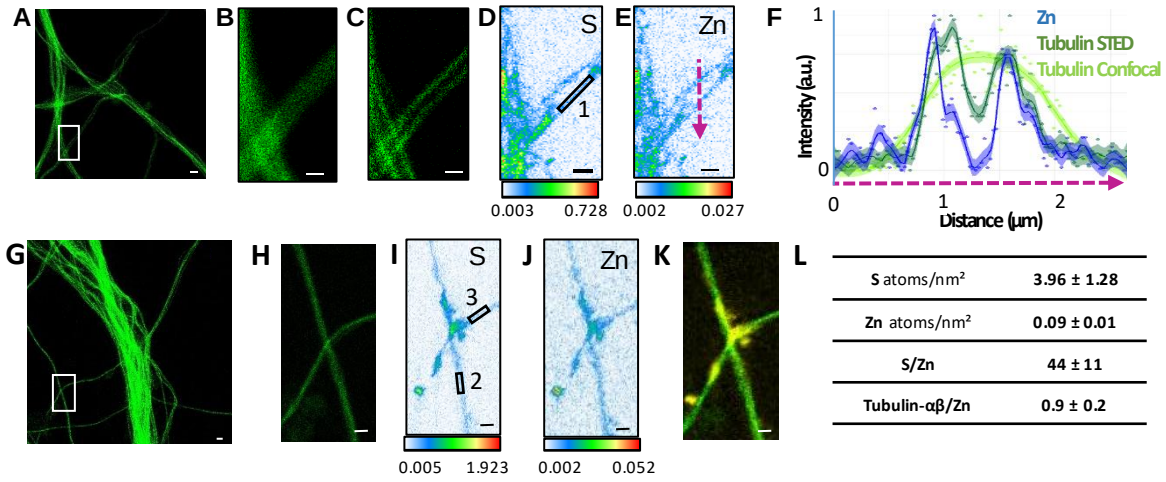

S atoms/nm²	3.96 ± 1.28
Zn atoms/nm²	0.09 ± 0.01
S/Zn	44 ± 11
Tubulin-αβ/Zn	0.9 ± 0.2

Fig. 4. Correlative STED and nano-SXRF imaging in dendrites. (A) STED image of SiR-tubulin (green). (B) Confocal SiR-tubulin image of the region framed in (A). (C) STED SiR-tubulin image of the region framed in (A). (D) Sulfur SXRF map. (E) Zinc SXRF map. (F) Plot profile of zinc (blue), STED SiR-tubulin (dark green), and confocal SiR-tubulin (light green) across two thin dendrites (magenta dotted line in E. (G) STED image of SiR-tubulin (green) in dendrites. (H) STED SiR-tubulin of the region framed in G. (I) Sulfur SXRF map. (J) Zinc SXRF map. (K) Overlay image of STED SiR-tubulin (green) and zinc distribution (yellow). (L) Quantitative data analysis of the number of sulfur and zinc atoms.nm^{-2} for 21 regions of interest centered on thin microtubules as illustrated for roi 1 to 3 framed in D and I (mean ± SD; n=21; see also Table S1). Scale bars: 500 nm, except for (A) and (G) 1 µm.

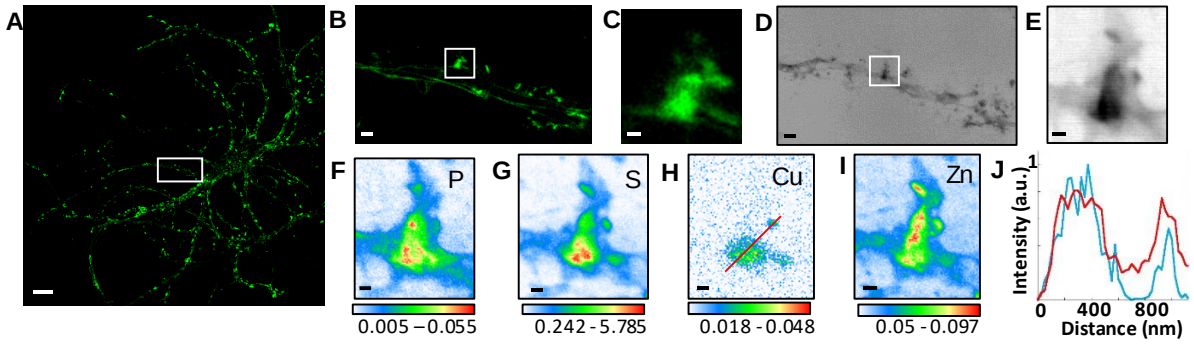

Fig. 5. Correlative STED microscopy of SiR-actin with synchrotron PCI and XRF in spines. (A) Confocal imaging of a primary rat hippocampal neuron labeled with SiR-actin showing F-actin-rich protrusions along dendrites. (B) STED imaging of SiR-actin of the dendrite region framed in white in A. (C) Zoom on the STED SiR-actin of a F-actin-rich protrusion framed in B. (D) Synchrotron radiation X-ray PCI of the dendrite region framed in white in A. (E) Zoom on the PCI region of a F-actin-rich protrusion framed in D. (F-I) SXRF element maps (P, S, Cu, Zn) from the region of interest framed in B and D. (J) Line scans for F-actin (red) and copper (blue) normalized distributions along the red line plotted in H. Scale bar: 200 nm, except for A 10 µm, B and D 1 µm. Color scales : min-max values in ng.mm^{-2}.

MATERIALS AND METHODS

Culture of primary rat hippocampal neurons

Cultures were done on silicon nitride (SN) membranes (Silson Ltd) consisting in square silicon frames of 5 x 5 mm² and 200 µm thickness with a central SN membrane of 1.5 x 1.5 mm² and 500 nm thickness. During manufacturing, a second, smaller (0.1 x 0.1 mm^2), SN membrane is added in one of the corners of the silicon frame to serve as orientation frame. Primary rat hippocampal neurons were dissociated from E18 Sprague-Dawley rat embryos (Janvier labs) and plated on the SN membranes treated with 1 mg.ml^{-1} poly-lysine (Sigma) in a 0.1 M borate buffer pH 8.5. The SN membranes were placed on an astrocyte feeder layer growing on a dish treated by 0.1 mg.ml^{-1} poly-lysine in a 0.1 M borate buffer pH 8.5, in Neurobasal medium (Gibco) as described in the protocol from Kaech and Banker (13). At 3-4 days *in vitro* (DIV3-4), the cells were treated with 2 µM of cytosine arabinofuranoside (Sigma) to limit the growth of the glial cells. From DIV6 and twice a week, half the Neurobasal medium was removed and

replaced by BrainPhys medium (STEMCELL) at 300 mOsm, a culture medium designed to respect neuronal activity for *in vitro* models (20). To develop dendritic spines, neurons were maintained in culture at 36.5°C in 5% CO_2 atmosphere until DIV15.

Cell labeling for STED and confocal imaging

For live-cell microscopy of tubulin and actin, cell permeable fluorogenic probes based on silicone rhodamine (SiR) from Spirochrome were used according to manufacturer instructions and published protocols (15, 21). The fluorophore stock solutions were prepared at 1 mM in DMSO. For single color STED imaging, DIV15 neurons were labeled by adding 1 µM of SiR-tubulin or 1 µM SiR-actin to the BrainPhys medium and neurons were exposed during 1.5h at 37°C. For dual color imaging 1 µM SiR-tubulin and 1 µM SiR700-actin were added together to the BrainPhys medium and neurons were exposed during 1.5h at 37°C.

STED and confocal imaging

Confocal and STED microscopy were performed on a commercial Leica DMI6000 TCS SP8 X microscope. DIV15 neurons cultured on SN membranes and labeled with SiR fluorogenic probes were maintained in the microscope chamber at 37°C in a Tyrode's solution (D-Glucose 1 mM, NaCl 135 mM, KCl 5 mM, $MgCl_2$ 0.4 mM, $CaCl_2$ 1.8 mM and HEPES 20 mM) pH 7.4 at 310 mOsm, the osmolarity of the BrainPhys culture medium. For live cell microscopy the SN membrane was mounted in a Ludin chamber. The SN membrane is placed on the glass coverslip of the Ludin chamber, with neurons facing the coverslip to minimize the distance between the objective and the cells to be observed. Confocal and STED images were acquired with a HC-PL-APO-CS2 93x immersion objective in glycerol with a numerical aperture of 1.3 and a scan speed of 400 Hz. SiR fluorogenic probes were excited at 640 nm (670 nm for SiR700) and the signal was detected with a Leica HyD hybrid detector with a window of emission recording from 651 to 680 nm for SiR and from 710 to 750 for SiR700. For STED acquisitions, the fluorescence outside the center was quenched with a 775 nm pulsed diode laser synchronized with excitation.

STED spatial resolution

The confocal lateral resolution was calculated as $\Delta d = \frac{0.4\lambda}{N.A}$ where Δd is the smallest resolvable distance between two objects and N.A. is the numerical aperture. For confocal microscopy, the lateral resolution calculated was 194 nm. The STED lateral resolution was calculated as $\Delta d = \frac{0.5\lambda}{N.A\sqrt{1+\frac{I}{I_{SAT}}}}$ with λ the emission wavelength and $\frac{I}{I_{SAT}}$ the saturation factor where I is the peak intensity of the depletion beam and I_{SAT} the saturation intensity corresponding to the value of half emission signal. With a λ emission wavelength for SiR-tubulin of 674 nm, a saturation factor $\frac{I}{I_{SAT}}$ between 34.5 and 57.5, and a N.A. of 1.3, the smallest distance between two objects that could be resolved was included between 32 and 44 nm. To fully exploit the spatial resolution of the STED setup (between 32 and 44 nm), the pixel size of STED images was set to 25 nm for oversampling the data.

Plunge-freezing and freeze-drying

Immediately after STED observations the neurons were plunge-frozen. Samples were quickly rinsed in a 310 mOsm ammonium acetate solution, pH 7.4 to remove extracellular inorganic elements present in Tyrode's solution that would interfere with nano-SXRF element mapping. The osmolarity of Tyrode's and ammonium acetate solutions were measured with a vapor pressure osmometer (VAPRO 5600, Elite) and adjusted to the initial values of the BrainPhys culture medium (310 mOsm). Then the cells were blotted with Whatman paper and plunge-frozen during 20 seconds in 2-methylbutane (Sigma) cooled down at -165°C in liquid nitrogen. Excess 2-methylbutane was carefully blotted with Whatman paper cooled in liquid nitrogen vapors and transferred in the freeze-drier. Neurons were freeze-dried in mild conditions, during 2 days at -90°C and 0.040 mbar in a Christ Alpha 1-4 freeze drier. Then the temperature and the pressure were slowly raised up to room temperature and ambient pressure and the samples were stored at room temperature within a desiccator until synchrotron analyzes.

Synchrotron nano X-ray Fluorescence microscopy (SXRF) and phase contrast imaging

Synchrotron experiments were performed on the ID16A Nano-Imaging beamline at the

European Synchrotron Radiation Facility (Grenoble, France) (6). The beamline is optimized for X-ray fluorescence imaging at 20 nm spatial resolution, as well as coherent hard X-ray imaging including in-line X-ray holography and X-ray ptychography. Featuring two pairs of multilayer coated Kirkpatrick-Baez (KB) focusing mirrors, the beamline provides a pink nanoprobe ($\Delta E/E \approx 1\%$) at two discrete energies: E = 17 keV and 33.6 keV. Despite the larger focus at lower energy, for the correlative STED-SXRF experiment 17 keV was chosen as it is more efficient in exciting the X-ray fluorescence of the biologically relevant elements. The X-ray focus with dimensions of 35 nm (H) x 57 nm (V) provided a flux of 3.7 10^{11} ph/s. The focus spot size was determined with a lithographic sample consisting of a 10 nm thick, 20 x 20 µm² square of nickel on a 500 nm thick SN membrane. The SN membranes holding the neurons were mounted in vacuum on a piezo nano-positioning stage with six short range actuators and regulated under the metrology of twelve capacitive sensors (22). An ultra-long working distance optical microscope was used to bring the sample to the focal plane (depth-of-focus ± 3 µm) and to position the STED regions of interest in the X-ray beam (see section sample positioning below). The samples were scanned with an isotropic pixel size of 40 nm, in some cases 20 nm for the scans of smaller size, and 100 ms of integration time. The X-ray fluorescence signal was detected with two custom energy dispersive detectors (Rayspec Ltd) at either side of the sample, holding a total of ten silicon drift diodes. The quantitative data treatment of the SXRF data was performed with Python scripts exploiting the PyMCA library (23), using the fundamental parameter method with the equivalent detector surface determined by calibration with a thin film reference sample (AXO DRESDEN GmbH). The resulting elemental areal mass density maps (units: ng.mm^{-2}) were visualized with ImageJ. The X-ray phase contrast imaging (PCI) exploits in-line holography. It is performed on the same instrument moving the sample a few millimeters downstream of the focus and recording X-ray in-line holograms with a FReLoN CCD based detector located 1.2 m downstream of the focus (24). X-ray holograms were collected in the Fresnel region at four different focus-to-sample distances to assure efficient phase retrieval. At each distance, images at 17 different lateral sample positions were recorded and averaged after registration, to eliminate artefacts related to the coherent mixing of the incident wavefront and the object. The neurons being pure and weak phase objects, phase retrieval was performed using the contrast transfer function approach (25), implemented in ESRF inhouse code using the GNU Octave language. The phase maps, proportional to the projection of the electron density, had a final pixel size

of 15 nm and a field of view of 30 x 30 μm^2. The spatial resolution was approximately 30 nm, similar to the STED and SXRF images.

Sample positioning

During STED microscopy the orthonormal coordinates (x,y) of the regions of interest are recorded according to three reference positions on the SN frame, 3 corners of the square SN membrane. The first reference position corresponds to the corner close to the 0.1 x 0.1 mm^2 orientation membrane, the second and third reference points to the corners selected from the first one in the clockwise direction. Using these 3 reference points the new coordinates (x',y') of the selected regions of interest can be calculated on the synchrotron ID16 setup using coordinate transformation equations.

Calculation of SXRF LOD

The limit of detection (LOD) obtained with the ID16A nano-SXRF setup was determined for the elements phosphorus, sulfur, potassium and zinc according to IUPAC guidelines (26).

$$LOD = m_{bi} + k \cdot \sigma_{bi} \qquad \text{(eq. 1)}$$

where m_{bi} is the mean of the blank measures, σ_{bi} is the standard deviation of the blank measures, and k is a numerical factor chosen according to the confidence level desired, k=3 for LOD. The resulting LOD values for each element based on the mean and standard deviation of 12 different blank analyses are presented in Table 1.

REFERENCES

1. A. M. Vergnano, N. Rebola, L. P. Savtchenko, P. S. Pinheiro, M. Casado, B. L. Kieffer, D. A. Rusakov, C. Mulle, P. Paoletti, Zinc dynamics and action at excitatory synapses. *Neuron* **82**, 1101-1114 (2014).
2. C. J. Chang, Searching for harmony in transition-metal signaling. *Nat. Chem. Biol.* **11**, 744-747 (2015).
3. Y. Hatori, Y. Yan, K. Schmidt, E. Furukawa, N. M. Hasan, N. Yang, C. N. Liu, S. Sockanathan,

S. Lutsenko, Neuronal differentiation is associated with a redox-regulated increase of copper flow to the secretory pathway. *Nat. Commun.* **7**, 1064 (2016).

4. T. Xiao, C. M. Ackerman, E. C. Carroll, S. Jia, A. Hoagland, J. Chan, B. Thai, C. S. Liu, E. Y. Isacoff, C. J. Chang, Copper regulates rest-activity cycles through the locus coeruleus-norepinephrine system. *Nat. Chem. Biol.* **14**, 655-663 (2018).
5. M. J. Pushie, I. J. Pickering, M. Korbas, M. J. Hackett, G. N. George, Elemental and chemically specific X-ray fluorescence imaging of biological systems. *Chem. Rev.* **114**, 8499-8541 (2014).
6. J. C. Da Silva, A. Pacureanu, Y. Yang, S. Bohic, C. Morawe, R. Barrett, P. Cloetens, Efficient concentration of high-energy x-rays for diffraction-limited imaging resolution. *Optica* **4**, 492-495 (2017).
7. S. Roudeau, A. Carmona, L. Perrin, R. Ortega, Correlative organelle fluorescence microscopy and synchrotron X-ray chemical element imaging in single cells. *Anal. Bioanal. Chem.* **406**, 6979-6991 (2014).
8. A. Carmona, C. E. Zogzas, S. Roudeau, F. Porcaro, J. Garrevoet, K. M. Spiers, M. Salomé, P. Cloetens, S. Mukhopadhyay, R. Ortega, SLC30A10 mutation involved in parkinsonism results in manganese accumulation within nanovesicles of the Golgi apparatus. *ACS Chem. Neurosci.* **10**, 599-609 (2019).
9. S. Watanabe, A. Punge, G. Hollopeter, K. I. Willig, R. J. Hobson, M. W. Davis, S. W. Hell, E. M. Jorgensen, Protein localization in electron micrographs using fluorescence nanoscopy. *Nat. Methods* **8**, 80-4 (2011).
10. M. Cosentino, C. Canale, P. Bianchini, A. Diaspro, AFM-STED correlative nanoscopy reveals a dark side in fluorescence microscopy imaging. *Sci. Adv.* **5**, eaav8062 (2019).
11. M. Bernhardt, J. D. Nicolas, M. Osterhoff, H. Mittelstädt, M. Reuss, B. Harke, A. Wittmeier, M. Sprung, S. Köster, T. Salditt, Correlative microscopy approach for biology using X-ray holography, X-ray scanning diffraction and STED microscopy. *Nat. Commun.* **9**, 3641 (2018).
12. L. Perrin, A. Carmona, S. Roudeau, R. Ortega, Evaluation of sample preparation methods for single cell quantitative element imaging using proton or synchrotron radiation focused beams. *J. Anal. Atom. Spectrom.* **30**, 2525-2532 (2015).
13. S. Kaech, G. Banker, Culturing hippocampal neurons. *Nat. Protocols* **1**, 2406-2415 (2006).
14. L. Perrin, S. Roudeau, A. Carmona, F. Domart, J. D. Petersen, S. Bohic, Y. Yang, P.

Cloetens, R. Ortega, Zinc and Copper Effects on Stability of Tubulin and Actin Networks in Dendrites and Spines of Hippocampal Neurons. *ACS Chem. Neurosci.* **8**, 1490-1499 (2017).

15. G. Lukinavičius, L. Reymond, E. D'Este, A. Masharina, F. Göttfert, H. Ta, A. Güther, M. Fournier, S. Rizzo, H. Waldmann, C. Blaukopf, C. Sommer, D. W. Gerlich, H. D. Arndt, S. W. Hell, K. Johnsson, Fluorogenic probes for live-cell imaging of the cytoskeleton. *Nat. Methods* **11**, 731-733 (2014).
16. J. H. Tao-Cheng, D. Toy, C. A. Winters, T. S. Reese, A. Dosemeci, Zinc stabilizes Shank3 at the postsynaptic density of hippocampal synapses. *PLoS One* **11**, e0153979 (2016).
17. J. Löwe, H. Li, K. H. Downing, E. Nogales, Refined structure of alpha beta-tubulin at 3.5 A resolution. *J. Mol. Biol.* **313**, 1045-1057 (2001).
18. W. Chowanadisai, D. M. Graham, C. L. Keen, R. B. Rucker, M. A. Messerli, Neurulation and neurite extension require the zinc transporter ZIP12 (slc39a12). *Proc. Natl. Acad. Sci. USA.* **110**, 9903-9908 (2013).
19. T. J. Craddock, J. A. Tuszynski, D. Chopra, N. Casey, L. E. Goldstein, S. R. Hameroff, R. E. Tanzi, The zinc dyshomeostasis hypothesis of Alzheimer's disease. *PloS One* **7**, e33552 (2012).
20. C. Bardy, M. Van der Hurk, T. Eames, C. Marchand, R. V. Hernandez, M. Kellogg, M. Gorris, B. Galet, V. Palomares, J. Brown, A. G. Bang, J. Mertens, L. Böhnke, L. Boyer, S. Simon, F. H. Gage, Neuronal medium that supports basic synaptic functions and activity of human neurons in vitro. *Proc. Natl. Acad. Sci. USA* **112**, E2725-E2734 (2015).
21. G. Lukinavicius, L. Reymond, K. Umezawa, O. Sallin, E. D'Este, F. Göttfert, H. Ta, S. W. Hell, Y. Urano, K. Johnsson, Fluorogenic probes for multicolor omaging in living cells. *J. Am. Chem. Soc.* **138**, 9365-9368 (2016).
22. F. Villar, L. Andre, R. Baker, S. Bohic, J. C. da Silva, C. Guilloud, O. Hignette, J. Meyer, A. Pacureanu, M. Perez, M. Salome, Nanopositioning for the ESRF ID16A nano-imaging beamline. *Synchrotron Radiat. News* **31**, 9-14 (2018).
23. V. A. Solé, E. Papillon, M. Cotte, P. Walter, J. Susini, A multiplatform code for the analysis of energy-dispersive X-ray fluorescence spectra. *Spectrochim. Acta B* **62**, 63–68 (2007).
24. R. Mokso, P. Cloetens, Nanoscale zoom tomography with hard x rays using Kirkpatrick-Baez optics. *Appl. Phys. Lett.* **90**, 144104 (2007).
25. P. Cloetens, W. Ludwig, J. Baruchel, D. Van Dyck, J. Van Landuyt, J. P. Guigay, M. Schlenker, Holotomography: Quantitative phase tomography with micrometer

resolution using hard synchrotron radiation x rays. *Appl. Phys. Lett.* **75**, 2912-2914 (1999).

26. IUPAC. *Compendium of Chemical Terminology*, 2nd ed. (the "Gold Book"). Compiled by McNaught AD and Wilkinson A (Blackwell Scientific Publications, Oxford, 1997).

Acknowledgments

We acknowledge P. Mascalchi and C. Poujol from Bordeaux Imaging Center, part of the France BioImaging national infrastructure, for support in microscopy; C. Breillat and N. Retailleau from IINS for neuronal cell culture; F. Porcaro from CENBG, for his help. **Funding.** This work was supported by a doctoral fellowship from the University of Bordeaux (F.D.), a grant from Centre National de la Recherche Scientifique (CNRS) Mission for Interdisciplinary Research (R.O.), a PEPS grant from CNRS and IDEX Bordeaux (R.O. and D.C.), a grant from CNRS IN2P3 Master Project IFI (R.O.), ERC grant ADOS (339541) and DynSynMem (787340) to D.C. and support fro the Regional Council Nouvelle Aquitaine. The synchrotron radiation experiments were performed in the frame of ESRF proposal LS2850 on beamline ID16A at the European Synchrotron Radiation Facility (ESRF), Grenoble, France. **Author contributions**: F.D., D.C., and R.O. designed the experiments. F.D. and E.V. designed and performed protocols for cell cultures. F.D., S.R., P.C., and R.O. performed synchrotron radiation experiments. P.C. developed nano-SXRF and PCI methodology. F.D., A.C., and P.C. performed data treatment of synchrotron radiation experiments. F.D. and R.O. performed STED experiments. F.D. analyzed STED experiments and S.R. provided advice. F.D., A.C., D.C. and R.O. wrote the manuscript. **Competing interests**: the authors declare no competing financial interests. **Data availability**. The data supporting the findings of this study are available from the corresponding author upon request. Synchrotron data are managed according to ESRF policy based on the PaNdata Data Policy.

SUPPLEMENTARY MATERIALS

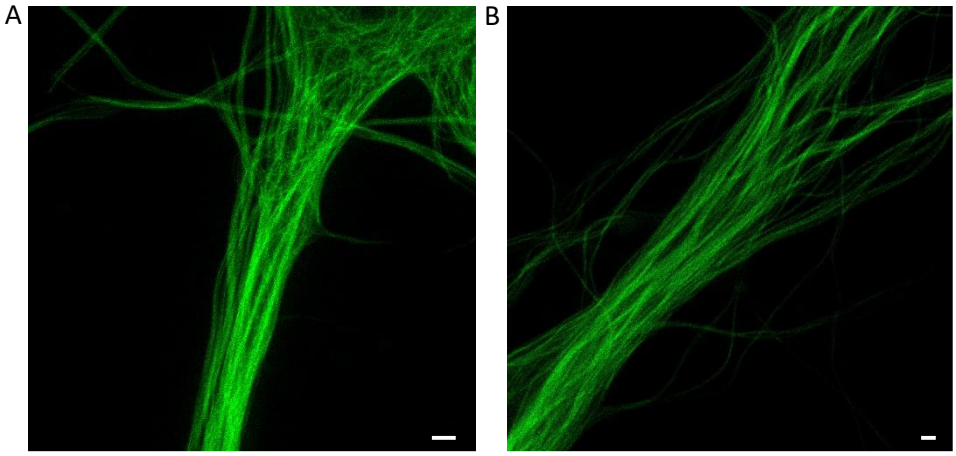

Fig. S1. Comparison of (A) STED imaging of SiR-tubulin of a dendrite from an hippocampal neuron grown on a glass coverslip and (B) STED imaging of SiR-tubulin of a dendrite from an hippocampal neuron grown on a silicon nitride membrane. Scale bars 1 µm.

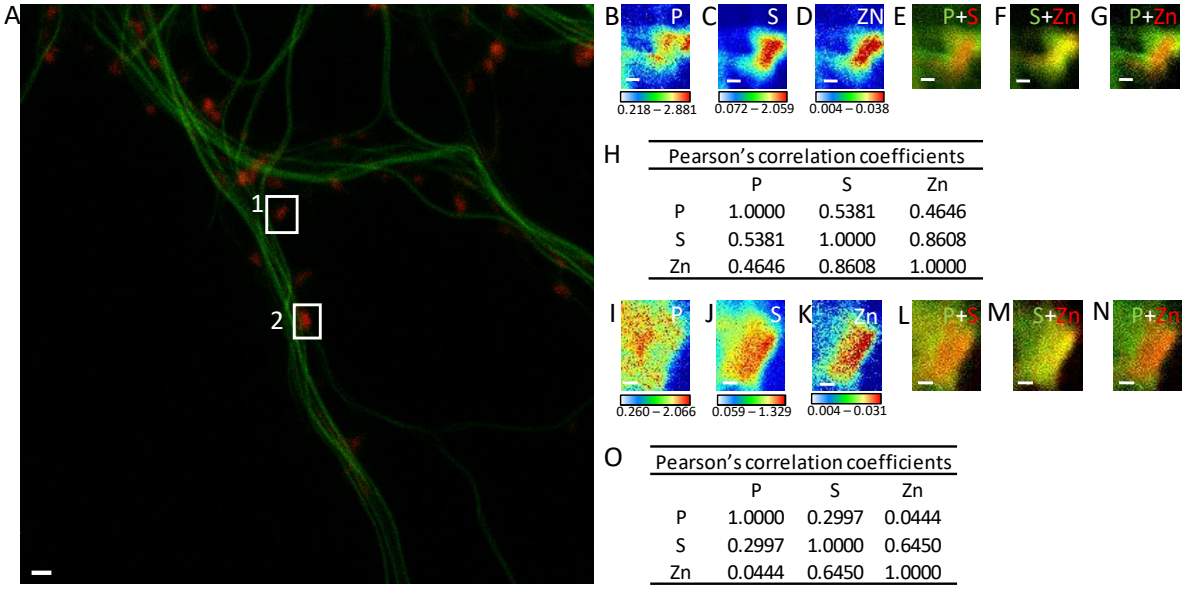

Fig. S2. Element distributions in dendritic spines. (A) STED image of SiR-tubulin (green) and confocal image of SiR700-actin (red). (B-D) SXRF element maps (P, S, Zn) from spine framed in (A) as region 1. (E) Overlay image of phosphorus (green) and sulfur (red). (F) Overlay image of sulfur (green) and zinc (red). (G) Overlay image of phosphorus (green) and zinc (red). (H) Pearson's correlation coefficients for the elements in spine 1. (I-K) SXRF element maps (P, S, Zn) from spine framed in (A) as region 2. (L) Overlay image of phosphorus (green) and sulfur (red). (M) Overlay image of sulfur (green) and zinc (red) . (N) Overlay image of phosphorus (green) and zinc (red). (O) Pearson's correlation coefficients for the elements in spine 2. Scale bars 200 nm except for (A) 1 µm. Color scales : min-max values in ng.mm^{-2}.

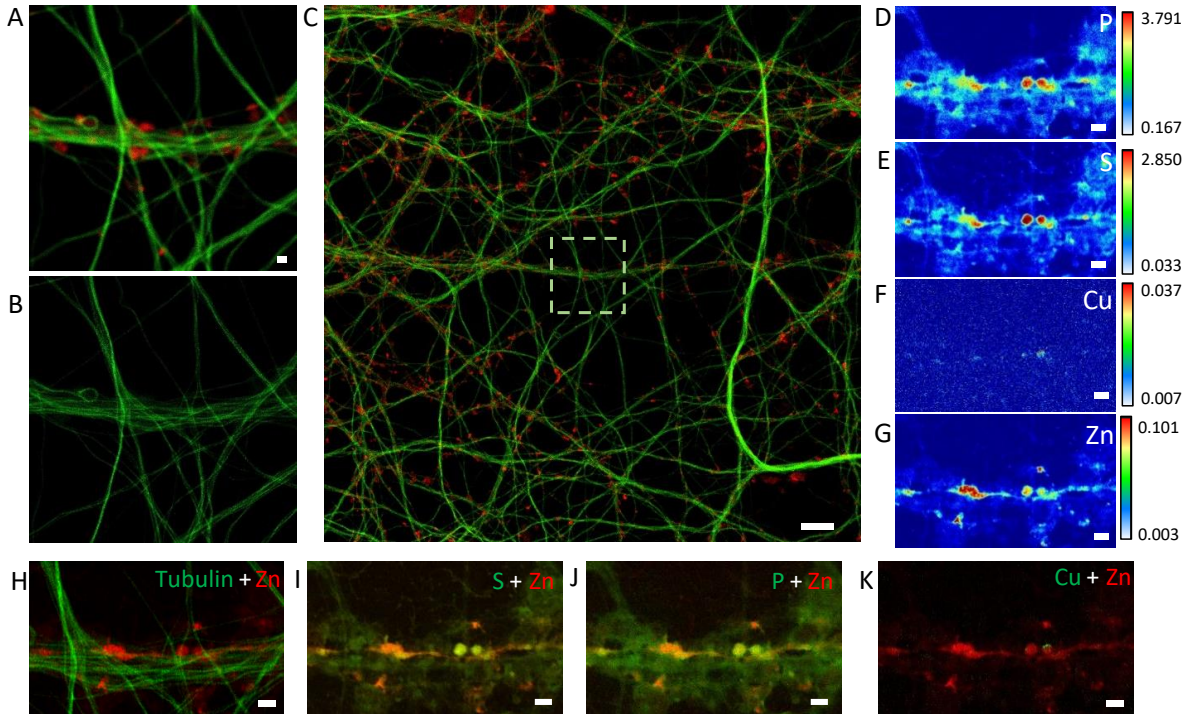

Fig. S3. Element distributions in dendrites and spines. (A) Confocal image of SiR-tubulin (green) and SiR700-actin (red) in dendrites. (B) STED image of SiR-tubulin in the same zone as in (A). (C) Confocal large image including the region shown in (A) with SiR-tubulin (green) and SiR700-actin (red). (D-G) SXRF element maps (P, S, Cu, Zn) from the same region as (A). (H) Overlay image of STED SiR-tubulin (green) and zinc (red). (I) Overlay image of sulfur (green) and zinc (red). (J) Overlay image of phosphorus (green) and zinc (red). (K) Overlay image of copper (green) and zinc (red). Scale bar: 1 µm except for (C) 10 µm. Color scales : min-max values in ng.mm^{-2}.

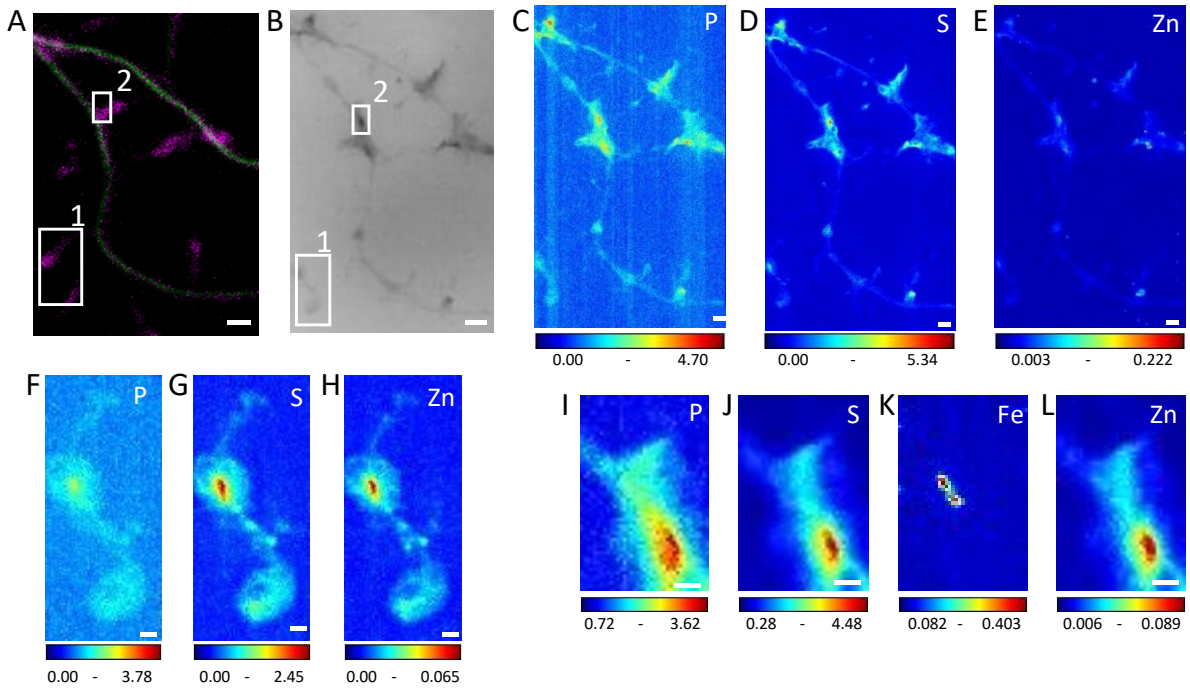

Fig. S4. Multimodal imaging of dendrites and spines. (A) STED SiR-tubulin (green) and confocal SiR700-actin (magenta) (B) Synchrotron radiation X-ray PCI of the same area as (A). (C-E) SXRF element maps (P, S, Zn) from the same region as (A) and (B). (F-H) SXRF element maps (P, S, Zn) from the framed region 1 in (B). (I-L) SXRF element maps (P, S, Fe, Zn) from the framed region 2 in (B). Scale bars: 200 nm, except (A) and (B) 1 µm. Color scales min-max values in ng.mm^{-2}.

Table S1. Nano-SXRF quantitative data. Analysis of chemical elements content for 21 regions showing zinc and tubulin co-localization, expressed in ng.mm^{-2} and in atoms.nm^{-2} (mean ± SD, n=21).

	Phosphorus	**Sulfur**	**Potassium**	**Zinc**
ng.mm^{-2}	0.600 ± 0.085	0.211 ± 0.068	0.153 ± 0.034	0.0105 ± 0.005
atoms.nm^{-2}	11.81 ± 3.29	3.96 ± 1.28	2.57 ± 1.23	0.09 ± 0.01